UNIVERSITY OF GRONINGEN

BACHELOR RESEARCH PROJECT PHYSICS

PET-verification in proton therapy

Characterization of in-beam scintillation detectors for nitrogen-12 imaging in proton beam radiotherapy

Author
Lucas GOEYENBIER (S3007081)

Supervisor
Peter DENDOOVEN
Second examiner
Emiel VAN DER GRAAF

Abstract

In this work, the required amount of protons needed to obtain a specific accuracy in the detection of $4.44 MeV$ gamma rays in a carbon target has been determined for different parameters. With this information, a beam time plan can be composed to execute this experiment. This experiment is useful for the development of Positron Emission Tomography (PET)-verification in proton therapy and could compensate for the uncertainties proton therapy entails. Furthermore, the behavior of a PET detector was analysed when it was switched off and on. The recovery period of the PET detector can be divided into two phases. In the fast recovery period, which is about $0.5 ms$ after the detector has been switched back on, the signal is unstable. In the beginning of the slow recovery period, which has a duration of approximately $25 ms$, the $511 keV$ photon peak was positioned at a value of $488.1 keV$ and this peak moves during the recovery slowly back to its original position.

rijksuniversiteit groningen

July 3, 2020

Contents

1 Introduction **2**

2 Materials and Methods **4**
2.1 Experimental setup $4.44MeV$ Gamma-ray detection 4
2.2 PET setup for verification of proton therapy 5
2.3 Scintillation detectors 7
2.3.1 Scintillators 7
2.3.2 Inorganic scintillators 7
2.4 Photomultiplier Tube (PMT) 8
2.5 Detector efficiency 9
2.6 Cross Section 9
2.7 Branching ratio 10
2.8 Production ^{12}N in a carbon target 10
2.9 Difference in production with and without carbon target 11
2.10 Mesytec software 11

3 Results **14**
3.1 Determination of the number of protons needed in a beam to obtain a specific relative accuracy 14
3.1.1 Measuring the proton energy as function of depth in water 14
3.1.2 Gamma ray production in carbon detected 14
3.1.3 Gamma ray production in water detected 15
3.1.4 Required number of protons for a specific accuracy for different parameters 15
3.2 Analysing the behavior of two PET detectors when switched off and on . . 15
3.2.1 Energy calibration 15
3.2.2 2D plots for different ^{68}Ge sources 17
3.2.3 Analysing the recovery effect for different energy windows 18
3.2.4 Analysing the behavior of the PET detectors in the recovery period . 19

4 Discussion **22**
4.1 Beam time plan for the detection of $4.44MeV$ gamma rays 22
4.2 Determination of the proton energy as a function of depth in water 22
4.3 The $^{12}C(p,n)^{12}N$ Cross section 22
4.4 Region in water for which the NaI detector can measure $4.44MeV$ gamma rays 22
4.5 Analysis of the behavior of the PET detectors 23
4.6 Determination of the 511 keV peak for slow recovery 23

5 Conclusion **23**

6 Acknowledgements **24**

7 Appendix **27**
7.1 Gaussian fitting for the calibration 27
7.2 Determination of the $511keV$ peak for the slow recovery 28

1 Introduction

Radiation therapy is one of the possibilities used to treat cancer. Radiation therapy is based on emitting radiation in the patient, resulting in deposition of energy due to atomic and nuclear interactions. These interactions can damage (tumor)cells and will eventually kill the cell. The amount of energy deposited by ionizing radiation, named the treatment dose, is measured in Gray (Gy) (J/kg) [9] .

The energy deposition can be done with different particles, for example photons, carbon ions and protons. Using protons for radiation therapy has the advantage that the radiation can be delivered more precisely than with photons [6] . Photons deposit their energy gradually, while protons have a "Bragg" peak [9]. The stopping power of protons increases as the proton energy decreases. Consequently, as the proton slows down, the energy deposition will increase per distance travelled. Finally, the proton energy will be so small that the proton comes to rest. The deposition of energy is done by different interactions. As the particles move, there will be four interactions where energy is lost: inelastic collisions with atomic electrons and nucleus and elastic collisions with atomic electrons and nucleus [1]. The dose delivery has its maximum at the end of their trajectory, earlier mentioned the Bragg peak. Because protons with a higher energy will travel a longer distance, the Bragg peak will be at a further distance. By using multiple protons with different energies, a range of Bragg peaks can be made to target the tumor of a specific size. The difference in dose delivery between a photon beam, mono-energetic proton beam and multi-energetic proton beam can be seen in figure 1 [6]. A photon beam has the highest dose at the entrance of the tissue, and less than 50% at the target region, while the proton beams have their maximum at the target region, given that the proton has the appropriate starting energy. Therefore, proton therapy has always a lower integral dose for a specific target dose than photon therapy [23].

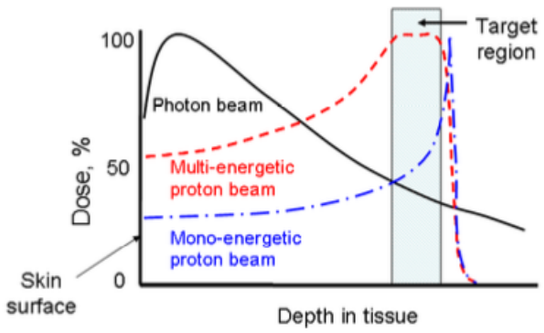

Figure 1: Dose delivery for a photon beam, mono-energetic proton beam and multi-energetic proton beam [6].

By choosing the right multi-energetic proton beam, functional treatment plans can be composed to optimize the radiation dose in the target region. Additionally, minimization of healthy tissue dose is wanted for limiting post-treatment complications. Besides, proton therapy delivers less dose to healthy tissue in front of the tumor and behind the tumor. The integral dose of proton therapy is approximately 60 percent lower than photon therapy [6]. However, the uncertainties in proton therapy are higher than in photon therapy. Specifically the range inaccuracy is a point to improve in proton therapy. In radiation therapy, it is required to kill all tumor cells. Otherwise, if leaving a few alive, the tumor will eventually return. Before undergoing proton therapy, a treatment plan will be drawn up. This is mostly done using a CT scan. The treatment plan contains the number of beams, directions at which the beam is oriented and the amount of dose delivery [9]. However, in this treatment plan, several uncertainties are included [21]. The CT image can possibly contain noise and distortions. Furthermore, during the radiation therapy, the target region can move due to the patient breathing. Because of this, the chance is higher to leave a part of the tumor without any radiation (under-shooting) or hit a healthy part with a full dose of radiation (over-shooting) in proton therapy. Because of this uncertainty, proton therapy is not always favoured over photon therapy. Therefore, new innovations are needed in proton therapy.

A possible solution to the under- and over-shooting problem would be to use a Positron Emission Tomography(PET) scan during the proton therapy, and is called PET verification.

The proton beam will interact with the elements present in the body. This interaction will create radioactive isotopes in the patient. Eventually the radioactive isotopes will decay and emit positrons. The positrons will annihilate with the electrons, creating two photons. The photons get detected by a PET-detector and the detector will image the irradiated part of the body. On the other hand, the disadvantage of using PET-verification is the decay time of most radioactive isotopes created by the proton beam, which is several minutes. This is too long to wait for during radiation therapy. However, a topic of interest is ^{12}N, which has a decay time of $11ms$. The most dominant atoms present in soft tissue are ^{11}C , ^{13}N and ^{15}O. When a proton beam will hit a carbon target, ^{12}N might be created [17]. Because of the low decay time, ^{12}N could start positron-electron annihilation quickly. The $511keV$ photons created in this annihilation are used for PET-verification in patients. However, ^{12}N could also decay and emit $4.44MeV$ gamma rays. Because the detection of $511keV$ photons created by positron-electron annihilation cause blurring images for this research, $4.44MeV$ gamma rays are detected [5]. This could be explained due to the fact that the positrons emitted in the decay of ^{12}N have relative high energies. The positrons will in most cases annihilate with electrons when they have come to rest. The root mean square distance for these positrons in water is approximately $20mm$. Therefore, the PET detector will measure the $511keV$ photons created by the positron-electron annihilation at a blurring distance of $20mm$.

In this research, the production of ^{12}N as function of depth for a proton beam in water is determined. In addition, an analysis was done of how many protons are required to achieve a specific accuracy for the number of $4.44MeV$ gamma rays detected with a NaI detector. This analysis is needed to make a beam time plan. The beam time plan consists among other things of the time of irradiation and the intensity of the beam. This has been done for an initial proton beam of $190MeV$, having a carbon target at a depth of $220mm$ in water. The energy of the proton beam as function of depth in water has been determined. A graph for the production rate of ^{12}N as function of depth was made. This was done for different thicknesses of carbon targets. Additionally, an estimation for the cross section of water was made in this calculation. Finally, the required amount of protons needed to achieve an accuracy of 1, 3 and 10% has been determined.

Secondly, the recovery time of a PET system has been analysed when it is switched off for $10ms$ and turned back on. By using the measurements of a ^{22}Na source, a calibration was made. Additionally, the behavior of the two PET detectors was analysed for a ^{68}Ge point source, line source and two identical line sources with point source. For different energy windows, the recovery effect was investigated. Finally, the position of the $511keV$ peak was determined for various times in the recovery period.

2 Materials and Methods

2.1 Experimental setup $4.44MeV$ Gamma-ray detection

For the detection of $4.44MeV$ gamma rays with a NaI detector, a schematic setup can be seen in figure 2 [28].

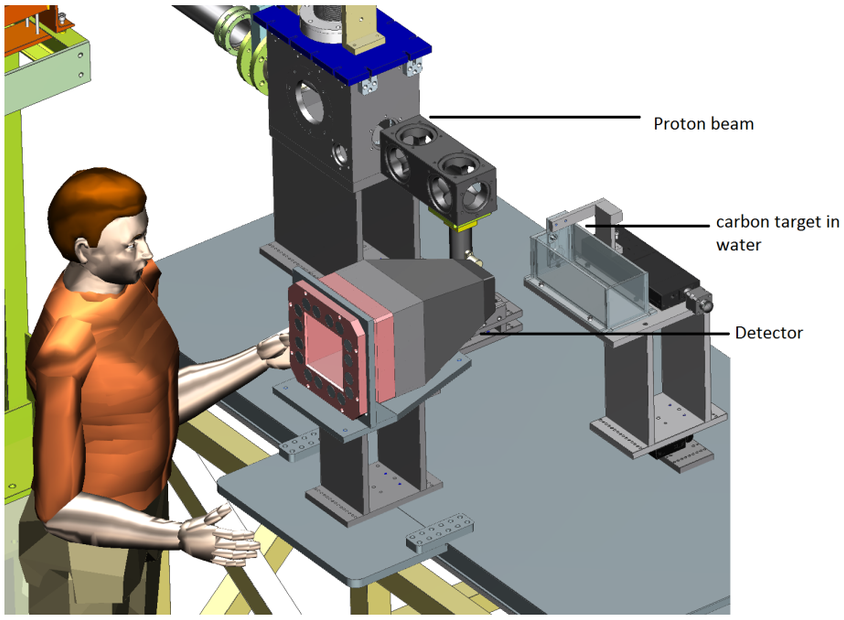

Figure 2: Experimental setup $4.44MeV$ gamma ray detection [28].

A proton beam with a starting energy of $190MeV$ will go through a box filled with water. A carbon target will be placed inside the box. The target used in this experiment is made of graphite material, having a density of $1.8g/cm^3$. There are three different targets thicknesses of 0.5, 1 and 2 mm respectively. A thinner target will obtain a better image resolution. However, it pays its price at the beam time needed to obtain the required amount of protons. The proton beam will interact with the water and carbon target. In this reaction, the radioactive isotope ^{12}N might be created. ^{12}N has a decay time of $11ms$ and undergoes β^+ decay. The branching ratio that ^{12}N will decay into the first excited state of ^{12}C is 1.9%. More explanation about the branching ratio is provided in section 2.7. The first excited state of ^{12}C has an energy of $4.44MeV$ [24]. There is a 100% chance that ^{12}C in the first excited state decays to the ground state, emitting a $4.44MeV$ gamma ray. This decay from the first excited state into the ground state has a half life of $2 * 10^{-14}s$ [25]. These gamma rays will be measured by a detector and provide information about the production of ^{12}N in carbon and water. The detector will be placed perpendicular to the proton beam. The detector used in this experiment is the Scionix 91x91x150mm NaI detector in the Eurogam Clover detector housing [Du99, E101, E103, EU02, Va16] [5]. The detector will be stationed approximately at a distance of $25cm$ from the carbon target. Additionally, the detector consists of a BGO compton suppression shield, which functions as housing. Inside the housing, a NaI detector is present. The dimensions of the NaI detector are 91x91x150mm. In figure 2, only the detector housing is shown. In section 2.3, more information is provided on scintillation detectors. An image of this NaI detector inside the housing is shown in figure 3 [28]. The efficiency of the detector is discussed in section 2.5. The carbon target will be moved in the water. Because the energy of the proton beam reduces as it moves in the water box, the carbon target can be placed at different distances in the water to obtain measurements at different energies. By doing this, a graph with the number of counts can be made as function of depth. This information is useful for the development of proton therapy. The proton beam is created at the AGOR cyclotron of the KVI-Center for advanced Radiation at the University of Groningen.

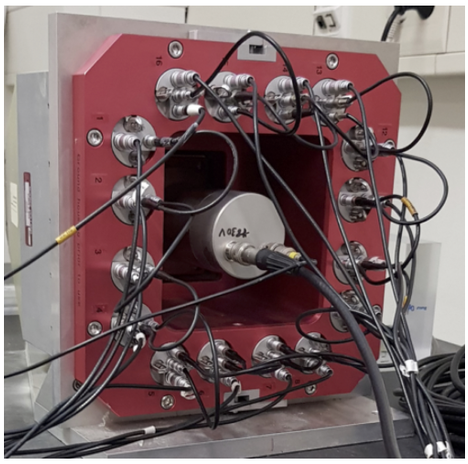

Figure 3: NaI detector inside Eurogam Clover detector housing [28].

^{12}N is potentially also produced on water. However, the cross section is not known. It is at least 10 times smaller than the cross section of carbon [17]. More information about the cross section is provided in 2.6. Furthermore, the region for which the detector measures gamma rays is unknown. A schematic drawing of the gamma ray detector can be seen in figure 4 [5].

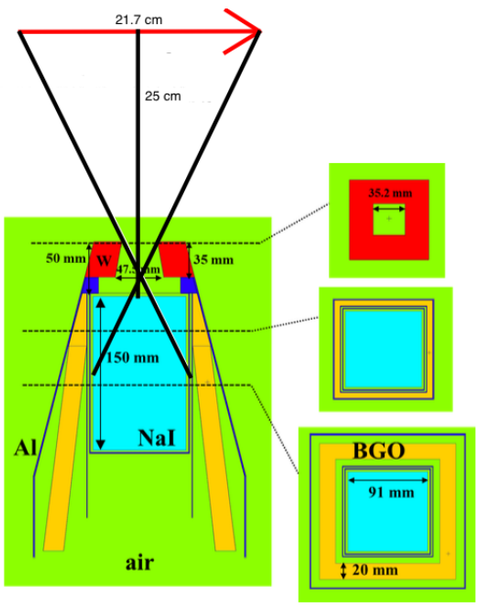

Figure 4: Schematic drawing gamma ray detector [5]. Two black lines were drawn to estimate the region for which the detector can measure gamma rays.

As can be seen from the figure, two black lines were drawn from sides of the NaI detector, moving past the edge of the housing and eventually end at an absolute distance of 25cm from the NaI detector. The red arrow indicates the distance between the two lines. This is also the path of the proton beam. Therefore, the distance of the red arrow has been measured to be around $21.7cm$. This is the region where the detector can measure gamma rays. However, this region is an indication and further research has to be done to determine the real region. The measurements for this research have been done for two different regions, namely 10 and 20 cm. The distance of this region is important because of the $4.4MeV$ gamma ray production in water.

2.2 PET setup for verification of proton therapy

For the second topic of this research, the behavior of a PET system was analysed when it is switched off and on. For this analysis, two PET detectors were used. One measurement loop had a duration of 100ms. During this loop, the detectors were shut down at 20ms and turned back on at 30ms. This loop was repeated until enough counts were detected. Five different measurements were performed. One measurement did not contain a source,

so only background radiation was measured. One measurement was done with a ^{22}Na source to make a calibration measurement. The last three measurements were done with ^{68}Ge sources. In particular, one measurement was done with a ^{68}Ge point source. Another measurement was done with a ^{68}Ge line source. The last measurement was done with two identical ^{68}Ge line sources and a ^{68}Ge point source. This was done with three different ^{68}Ge sources to obtain different count rates.

The information about the behavior of a PET scan is useful for the clinical implementation of in-beam PET verification. Firstly, the dose is delivered, where the proton beam irradiates the patient, resulting in ionization and excitation of atoms [6]. During this, the tumor cells will be killed. Furthermore, during the dose delivery, positron electron pairs will be created. These pairs will annihilate and create photons which will get detected and with this detection it can be checked if the dose was delivered at the right location. For Pencil Beam Scanning, the proton beam will be pulsed during a treatment of a patient. Immediately after the pulse, it can be checked if the energy deposition of the protons was delivered at the right position. The beam will be moved slightly after every pulse, to make a complete three dimensional dose distribution.

A method based on positrons for tomographic imaging is positron emission tomography (PET). This method requires positron emitting radionuclides. A positron can interact with an electron, creating positron-electron annihilation [12]. This interaction creates a photon annihilation pair, moving in mirrored direction from each other. Thereafter, the two photons get detected by a detector split up in small detectors. An example of the principle of a PET system can be seen in figure 5 [20]. The annihilation photons have an energy of $511keV$. This energy has a relatively low detector efficiency.

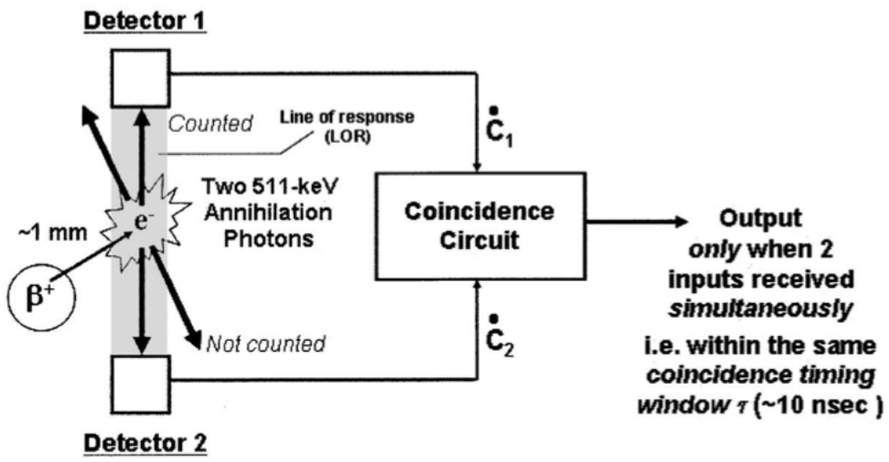

Figure 5: Working mechanism of a PET system [20].

Because the photons move in 180 degrees opposing direction having the same initial energy, the position of the original positron-electron annihilation can be determined along the line of the two detectors that register a simultaneous detection. Annihilation coincidence detection (ACD) is based on this mechanism, and does not use absorptive collimators. If two detectors record an event within a specific time, called the coincidence timing window, a coincidence event is expected to have happened. Uncertainties in the resolution can occur by the electronics and cables, conversion of 511 keV into a signal (light, electrons or electron-hole pairs) and the method to determine the time at which the interaction has taken place. The resolution is mainly described by a Gaussian, having the full width at half maximum (FWHM) [12].

It is possible to reconstruct the position of the annihilation by using time-of-flight PET. The equation for the time of flight PET is given by equation (1). Δt is in this equation the difference in arrival times of photons. Δd symbolizes the depth resolution.

$$\Delta d = \frac{\Delta t * c}{2} \tag{1}$$

There are three possible "prompt coincidences". They are shown in figure 6 [19]. Only one of them is the true coincidence, which is necessary to make a reliable image. The other two prompt coincidences create a false image. When one of the two photons in a back to

back annihilation is scattered, both photons will be detected within the coincidence timing window. However, because the photon was scattered, a different line of origin will be imaged. This is called a scatter coincidence. It is also possible that two photons, which are emitted from two different positrons annihilations, are detected within the coincidence timing window. This is called a random coincidence.

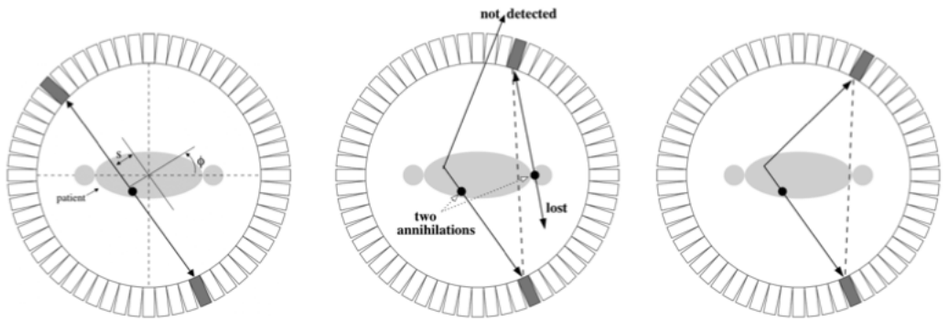

Figure 6: Three types of coincidence events. True coincidence (left), random coincidence (middle) and scatter coincidence (right). The last two coincidences will create a false image [19].

2.3 Scintillation detectors

2.3.1 Scintillators

Radiation which interacts with matter causes ionization or excitation in atoms [12]. The ionized or excited atoms can release this energy when deexcitation or recombination occurs. Most of this energy is released in the form of thermal energy. However, some materials are able to release this energy in the form of visible light, named scintillators. There is a proportional relation between the amount of energy deposited by incoming radiation and the amount of visible light energy released. In light of the working of a PMT (one visible photon creates one electron), the number of visible photons is more important than the total energy they represent. Radiation detectors are made from scintillation detectors. There are two types of scintillators, organic and inorganic respectively.

2.3.2 Inorganic scintillators

Inorganic scintillators consist of solids with a crystal structure. Scintillation is possible for these solids because of the properties of the crystal structure [14]. The detector used for the first topic is a NaI detector, which is a inorganic scintillator. For the second topic, an inorganic LSO scintillator was used. Electrons can only be in specific energy bands, if the crystal lattice is pure inorganic. These bands are called the conduction (excited) and valence (ground) band. The other energy bands are forbidden, and no electrons will be found there. The band structures for solids can be seen in figure 7 [15].

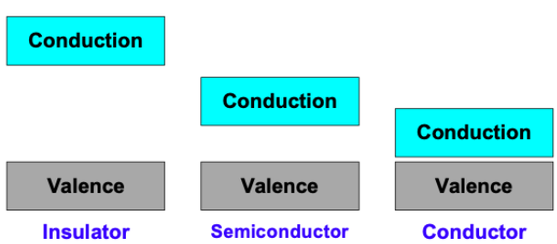

Figure 7: Band structures for crystal lattices [15].

Furthermore if the electrons in the lattice absorb energy, they can move from the valence band to the conduction band. This will result in a empty spot in the valence band. Eventually the electron will return to the valence band, by emitting a photon. This process is respectively inefficient, because only a few photons will be released, and they have an energy which is not within the spectrum of visible light. Therefore, impurities are added to the crystal. These "activators" modify the band gaps in the crystal lattice. In particular, the width between valence and conduction band is smaller because of the activator ground state and excited states in between the original bands. The difference of a pure crystal and

a crystal with impurities can be seen in figure 8 [15]. The energy structure of the crystal overall remains the same, however the energy states of the activator are different. Because the width in energy bands is smaller, the photons emitted have a lower energy, which is indeed in the visible range.

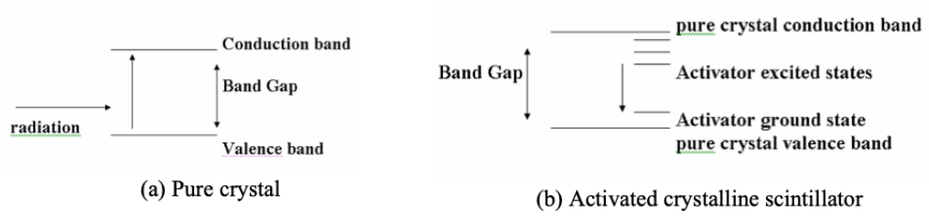

Figure 8: Difference in band structures between pure crystal (a) and activated crystalline scintillator (b) [15].

2.4 Photomultiplier Tube (PMT)

Photomultiplier tubes, named PMT, can produce an electric current pulse from an incoming weak signal [12]. The strength of this pulse is dependent on the intensity of the incoming particle. The weak signal can be in the form of a photon or β particle originating from a scintillator detector. A PMT is used in the PET system. The $511keV$ photons which are detected by a PET detector will be transformed into optical photons. This process takes place in a scintillation crystal and only a few optical photons will be created. This low number of optical photons characterizes the weak signal and gets transformed into a electrical current pulse by a PMT. A schematic setup of a PMT is given in figure 9 [18].

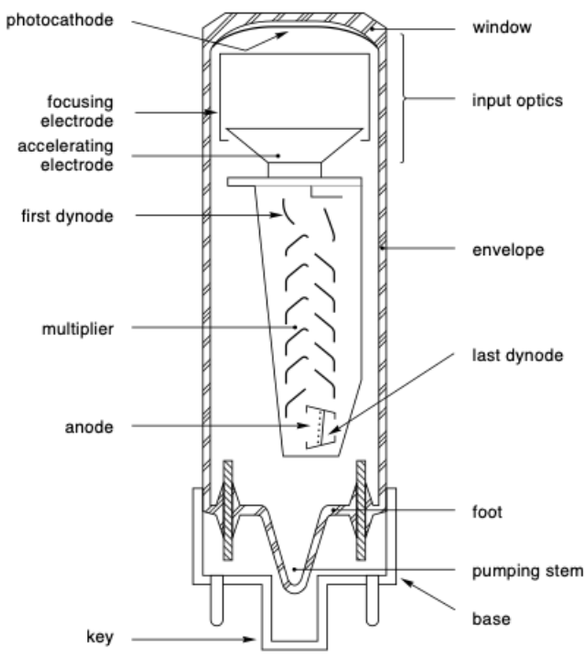

Figure 9: Elements of a photomultiplier tube based on the first fast PMT, made by Philips (nowadays Photonis) in 1956 [18].

The entrance of the PMT is coated with a material that ejects electrons when a photon of visible light hits the coating. This photoemissive coating is used as photocathode. Therefore, the photocatode ejects photoelectrons through the tube. Inside the tube are dynodes. The photoelectrons are attracted by the dynodes. The Dynodes have a positive voltage, mainly around 300V. When a photoelectron hits the dynode, several "secondary" electrons are ejected. The number of secondary electrons depends on the voltage difference between dynode and photocatode. Typical photomultiplier tubes have 9 to 12 dynodes and have a gain in the order of $1 * 10^6$. Every consecutive dynode has a higher voltage than the previous one. This will result in a multiplication of electrons, every time a dynode has been reached. Finally, the electron shower eventually ends at the anode, and a current is created.

For the analysis of the behavior of two PET detectors, the PET detectors were turned off for a short time. In this way, a PMT is pulsed [26] [27]. The PMT was switched off by shorting the circuit between photocathode and first dynode. A quick diode switch will short the circuit. The switch gets controlled by a 5 Volt square pulse from a waveform generator. By shorting the circuit, there is no potential difference over the first dynode and photocathode. The total voltage of the PMT, which is $-1350V$, remains. However this voltage will be across the first dynode and the anode. Because of the short circuit, the electrons created in the photocathode will not be accelerated to the dynodes. Therefore, electron multiplication will not occur and no signal will be created by the PMT. When the voltage returns across the full circuit, the PMT requires a short period of time to get a stable signal. Because the voltage is not directly back to its desired value, the electron multiplication process is not immediately stable. This recovery process has two phases. The first phase consists of approximately $0.5ms$ to obtain a proper pulse. The second phase, which takes between $20 - 25ms$ is required to return a stable gain in the PMT.

2.5 Detector efficiency

For the detection of $4.44MeV$ gamma rays, a NaI detector in the Eurogam Clover detector housing [Du99, E101, E103, EU02, Va16] will be used. The detector efficiency for gamma-rays of this detector has been determined by Emiel van der Graaf using Monte Carlo simulations [5] [22]. For the following photon energies, the detector efficiency is determined: 0.1, 0.2, 0.3, 0.4, 0.5, 0.511, 0.6, 0.662, 0.7, 0.8, 0.9, 1.0, 1.173, 1.25, 1.275, 1.332, 1.50, 1.75, 2.0, 3.0, 4.0, 5.0, 6.0, 7.0, 8.0, 9.0, 10.0 MeV . The efficiencies for the mentioned energies are given in figure 10 [5].

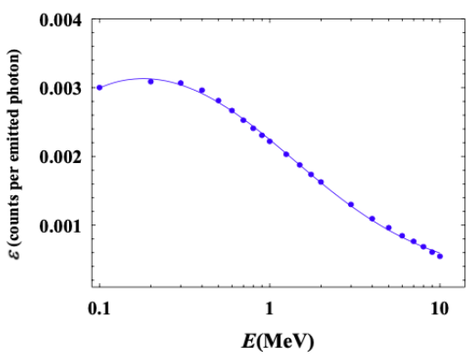

Figure 10: Detector efficiencies for the full energy peak for the NaI detector. The line is the fit made using equation (2) [5].

The uncertainty in the simulations was smaller than 1.0% for all data points. In addition, an equation has been made for the efficiency using a five-parameter rational function. This function is given by equation (2). In this equation, the parameters are as follow : $a = -0.009, b = 0.604, c = 0.022, d = 150.959, e = 123.013$.

$$f(x) = \frac{a + bx + cx^2}{1 + dx + ex^2} \tag{2}$$

For the detection of $4.44MeV$ gamma rays, equation (2) can be used to determine the detector efficiency for this energy. Therefore, by filling this in for x in equation (2), a detector efficiency of 0.001 is obtained.

2.6 Cross Section

The detection of $4.44MeV$ gamma rays falls in the category scatter experiments. A scatter experiment is defined as an experiment where a beam of particles hits a target, resulting in a production of various particles in the final state. This scatter experiment has different features. The flux density is given by equation (3) and is measured in $\frac{particles}{cm^2 * sec}$ [10]. In this equation, v_i (cm/s) is the velocity of the particles in the beam, measured from the rest frame of the target. The number density of particles in the beam is denoted by n_b $(particles/cm^3)$.

$$J = n_b * v_i \tag{3}$$

Using the flux, the rate W_r can be determined, where W_r denotes the rate at which a particular reaction r occurs in a specific experiment. The equation for this rate (s^{-1}) is given by equation (4).

$$W_r = J * N * \sigma_r \tag{4}$$

Where the amount of particles inside the target is noted as N. The symbol σ denotes the cross section for this reaction r. Therefore, by looking at equation (2), it can be seen that the cross section defines the probability that a specific reaction r will take place in a particular area. The unit for cross section is barn. One barn is equal to $10^{-28}m^2$. Since σ_r is the cross section for reaction r specificially, there is also a total cross section, denoted $\sigma_{tot} = \sum_r \sigma_r$. Since particles in experiments are scattered in different angles, the differential cross section terms could be used for this. The cross section in terms of differential cross section is denoted by equation (5).

$$\sigma_r = \int_0^{2\pi} d\phi \int_{-1}^{1} dcos\theta \frac{d\sigma_r(\theta, \phi)}{d\Omega} \tag{5}$$

The cross section has been determined with figure 11 [7]. This graph has results up to 48 MeV. The cross section is slowly decreasing from 24 to $48MeV$. Therefore, from energies ranging between 49 and 54 MeV, a slowly decreasing cross section to a value of $2mb$ was taken. From $54MeV$ until $190MeV$, a constant cross section of 2mb was taken.

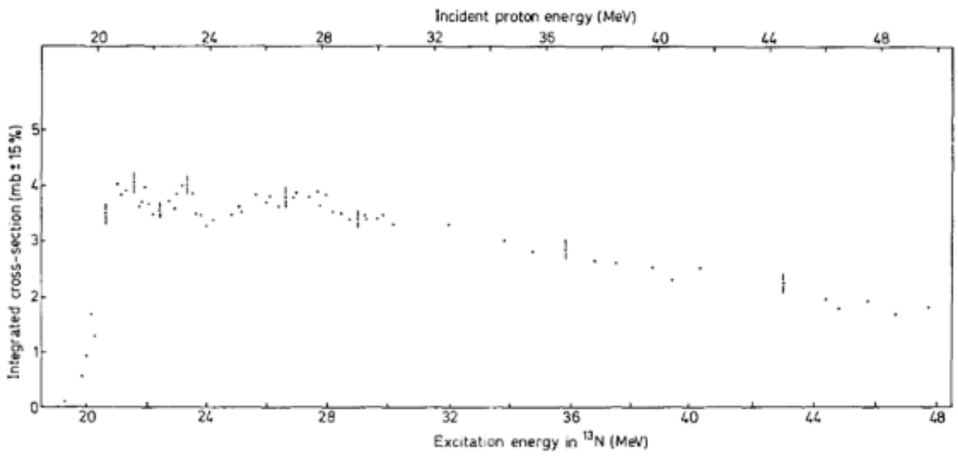

Figure 11: The 12C(p,n)12N Cross section [7].

The cross section for water for this reaction is unknown. However, it is definitely more than 10 times smaller than the cross section for carbon [17]. Therefore, in this experiment, this analysis was done for three different cross sections which are 10, 3 and 1% of the carbon cross section.

2.7 Branching ratio

If a particle is in an unstable state, it will eventually decay. The lifetime in the rest frame of the particle in question is denoted by τ . Using this lifetime, the decay width can be determined using $\Gamma = \frac{\hbar}{\tau}$ [10]. However, it happens that an unstable state will decay in several final states. The sum of all decay widths is the total decay width, denoted $\Gamma = \Sigma_f \Gamma_f$. The Branching ratio is defined as the probability that a particular decay f takes place, out of all possible decay states. Therefore, the branching ratio for a state f is denoted by $B_f = \Gamma_f / \Gamma$. The branching ratio for $4.44MeV$ gamma rays in ^{12}N is 1.9% [5].

2.8 Production ^{12}N in a carbon target

The stopping power of the proton beam in water and in carbon has been determined using [4]. The stopping power is defined as the sum of the electronic and nuclear stopping power, which stands for the amount of energy loss a particle experiences when moving through a specific material [8]. By using [4], the stopping power for different materials can be generated for the wanted energy levels. The stopping power is measured in units of $\frac{MeV*cm^2}{g}$. Since the topic of interest in this research is the Bragg peak, which is the point when protons have respectively low energies, higher interval steps have been taken at high energies. From 0 to $40MeV$, steps of $1MeV$ have been taken. From 40 to $120MeV$, steps of

$2MeV$ have been taken and from 120 to $190MeV$, stept of $5MeV$ have been taken. By using the density of water ($0.997g/cm^3$) and carbon ($1.8g/cm^3$), the energy loss per mm at a specific energy has been determined. In this experiment, it is important to know the energy of the proton at a specific depth in the water. Therefore, a graph has been made with proton energy as function of depth. This has been done by subtracting the energy loss per mm at the specific energy of the proton from the total energy of the proton. Since there have been taken steps varying from $1MeV$ to $5MeV$ in the stopping power table, the values have been rounded off. The production rate of ^{12}N is determined using equation (6). In this equation, ϕ is defined as the fluence, the total number of particles that forms the beam and is unitless. $N_{target}(cm^{-2})$ has been calculated using (7). In equation (7), d stands for the thickness of the target, M is the molar mass and N_a is the number of Avogadro.

$$P = \sigma * N_{target} * \phi \tag{6}$$

$$N_{target} = \frac{\rho * d * N_a}{M} \tag{7}$$

Using equation (6), the production of ^{12}N in the carbon target can be determined. This has been done for three different target thicknesses of 0.5, 1 and 2 mm. The amount of $4.44MeV$ gamma rays that is detected is equal to P, multiplied by the detector efficiency and the branching ratio. Furthermore, equation (6) and (7) are used for the determination of the production of gamma rays in water, since there is also a production of $4.44MeV$ gamma rays in water.

2.9 Difference in production with and without carbon target

In this experiment, two measurements are done. The first measurement is without carbon target. This means that the detector will only detect the gamma rays produced by the water which is in the sight of the detector. The second measurement is with target. Therefore, the detected amount of protons consists of a combination of carbon and water produced photons. In conclusion, M_1 defines the number of detected gamma rays exclusively produced in water, and M_2 is the number of detected of gamma rays produced in water and in the carbon target. Consequently, $M_2 - M_1$ is then the number of detected gamma rays particular for the carbon target. The error in a measurement set is equal to the square root of the amount of counts, assuming that this statistical error is dominant. This means that $\Delta M_1 = \sqrt{M_1}$ and $\Delta M_2 = \sqrt{M_2}$. The error in the difference of two measurements ($Z = A \pm B$) is $(\Delta Z)^2 = (\Delta A)^2 + (\Delta B)^2$ [11]. Therefore, the error in the amount of counts for in carbon produced gamma rays is given by equation (8).

$$\Delta(M_2 - M_1) = \sqrt{(\Delta M_2)^2 + (\Delta M_1)^2} = \sqrt{(\sqrt{M_2})^2 + (\sqrt{M_1})^2} = \sqrt{M_1 + M_2} \tag{8}$$

The relative error is given by equation (9).

$$\frac{\Delta(M_2 - M_1)}{M_2 - M_1} = \frac{\sqrt{M_1 + M_2}}{(M_2 - M_1)} \tag{9}$$

By using equation 9, an expression can be made for the amount of protons needed for a particular accuracy. This results in the following expression : $F = \frac{(\frac{\sqrt{M_1+M_2}}{(M_2-M_1)})^2}{A^2}$, where F is the amount of protons required and A is the relative accuracy wanted.

2.10 Mesytec software

The software used for analysing the behavior of two PET detectors was done with Mesytec. The mvme program was used, which is a VME data acquisition and analysis system. The program is illustrated in figures 12 and 13. The software can be installed for free. However, the source code is unavailable. In addition, the detectors were pulsed. The duration of the loop was $100ms$, where the detectors were switched off at $20ms$ and switched on at $30ms$. This loop was repeated until enough measurements were taken. The data contains the energy and timestamp for both detectors. A measurement set(listfile) can be loaded and replayed with energy or time window filters to analyse the behavior of the two PET detectors.

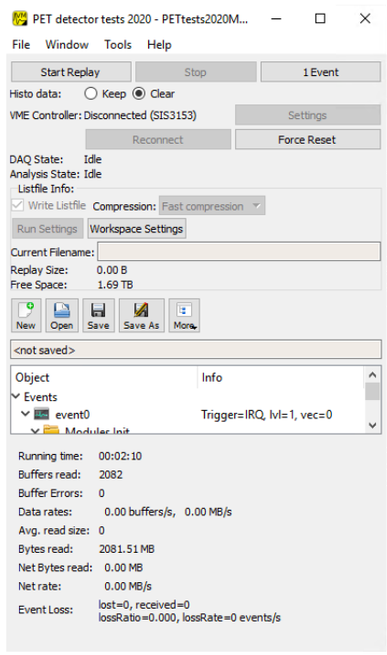

Figure 12: VME Mesytec listfile player.

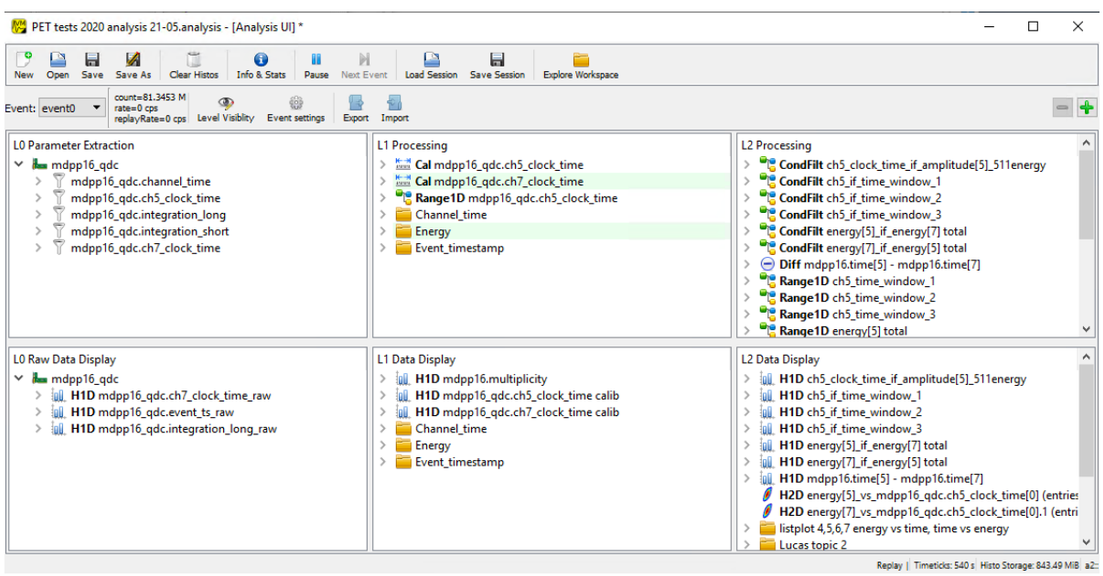

Figure 13: VME Mesytec data acquisition analyser.

A measurement set, named listfile, can be loaded with the program shown in figure 12. The analysis can be done with the data acquisition system (DAQ) shown in figure 13. The DAQ provides the possibility to make 1D range filters in the L2Processing section. The range filters can contain either energy or time window filters. Furthermore, condition filters can be made, giving a condition to a 1D range filter. 1D and 2D histograms can be made using L2 Data Display. 1D histogram data can be saved as a txt file and exported. However, 2D histograms can only be saved as PDF, and therefore not imported in different programs. An example of a 1D histogram txt file can be seen in figure 14.

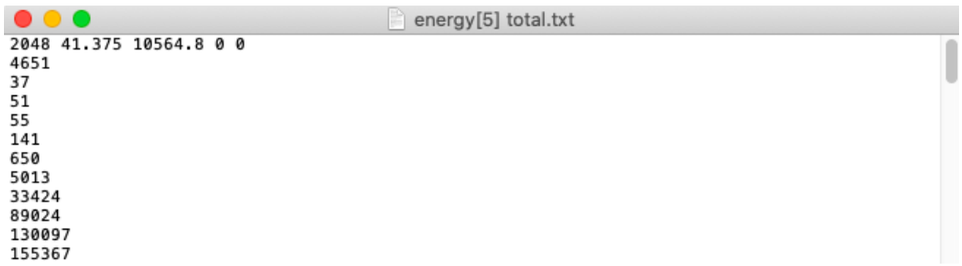

Figure 14: VME Mesytec data acquisition analyser. The first row consists of the following numbers: 2048 (11 bits), 41.375 (starting point x-axis), 10564 (end point x-axis), 0 , 0. The column under the first row denotes the y-values.

The first row provides the following information: "number of measurements, x_{min}, x_{max}, 0, 0". Under the first row, one column with all y-values is given for consecutive x-values respectively. The text files were imported into Python and Matlab to plot the graphs.

3 Results

3.1 Determination of the number of protons needed in a beam to obtain a specific relative accuracy

3.1.1 Measuring the proton energy as function of depth in water

Using [4] , the stopping power for a proton beam in water was found. Therefore, the following graph can be obtained for the energy of the proton as a function of depth. It can be seen from the graph that the proton is at rest between 244 and 245 mm.

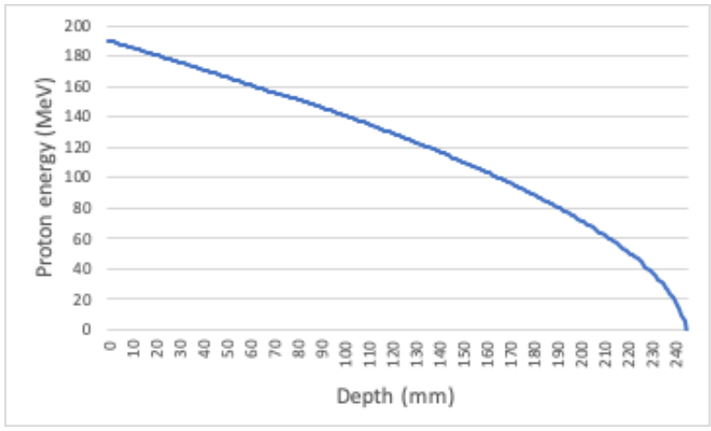

Figure 15: The Proton energy as function of depth in water.

3.1.2 Gamma ray production in carbon detected

Using equation (7), the amount of atoms in the target have been determined for three targets, having a thickness of 0.5, 1 and 2 mm. The values $4.51 * 10^{21}$, $9.02 * 10^{21}$ and $1.80 * 10^{22}$ (cm^{-2}) were obtained respectively. Using the cross section from figure 11, and taking a value of $1 * 10^{6}$ for the fluence, the production rate for the three targets was determined. These values are multiplied by the detector efficiency measured by Emiel van der Graaf and the branching ratio, which is 1.9%. This results in the amount of gamma rays, having a energy of $4.44 MeV$, which are detected by a NaI detector. This is given in figure 16. The number of gamma rays that is detected is per $1 * 10^{6}$ proton beam particles.

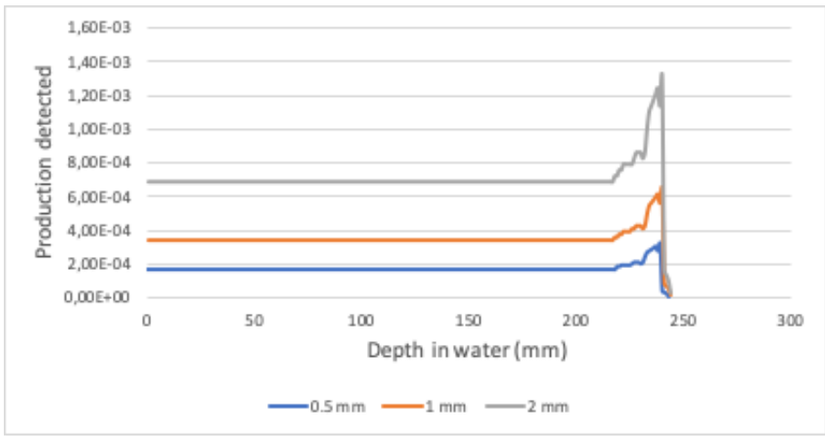

Figure 16: The production of 4.44 MeV gamma rays in carbon detected as a function of depth for three different carbon thicknesses (0.5, 1, 2mm).

Since the cross section for an energy higher than $54 MeV$ has been set constant, the production detected is constant for these values. Because the interest is in the Bragg peak, this is no issue for further results. The difference between the different targets is a factor 2 and 4 respectively. Beside the thickness difference, the parameters for the production detected are identical. The peak of the graphs in figure 16 is positioned at a depth of $228 \pm 1 mm$.

3.1.3 Gamma ray production in water detected

The production rate detected in water has been determined for three different cross section assumptions, namely a factor $0.1, 0.03, 0.01$ of the cross section of carbon. The value for N_{target} for water has been determined with equation (7). Since the only atoms in water of interest are oxygen, the mass of oxygen in water has been taken. The results for the detected production are given per $1 * 10^6$ proton beam particles. At a depth of $220mm$, the production of $4.44MeV$ gamma rays detected in water with a region of $10cm$ is 0.00124, 0.000373 and 0.000124 for cross sections of a factor 0.1, 0.03 and 0.01 of the cross section of carbon. For a region of $20cm$, this production detected at a depth of $220mm$ is 0.00248, 0.000745 and 0.000248 for cross sections of a factor 0.1, 0.03 and 0.01 of the cross section of carbon. This was done for these two region values because the region of the detector is uncertain, but the boundaries will lie presumably between these two values. Furthermore lead shielding could be placed in between the detector and the water box to prevent gamma rays originating from the water to get detected.

3.1.4 Required number of protons for a specific accuracy for different parameters

In the experiment, two measurements will be done, one without and one with carbon target. Therefore the first measurement will result in the production of gamma rays only due to water, and the second measurement consists of a combination of water and carbon produced gamma rays. The different parameters in this experiment are the thickness of carbon target, thickness of water region, the weighted factor of cross section in water and the relative accuracy wanted. Table 1 shows the required amount of protons needed to obtain this accuracy for all different parameters. These results can be used to make a beam time plan to physically execute the experiment.

Table of accuracy			Relative accuracy		
Water region thickness (cm)	Cross section (factor of carbon CS)	Carbon thickness (mm)	1%	3%	10%
20	0.1	0.5	$1.44 * 10^{15}$	$1.60 * 10^{14}$	$1.44 * 10^{13}$
20	0.1	1	$3.73 * 10^{14}$	$4.15 * 10^{13}$	$3.73 * 10^{12}$
20	0.1	2	$9.99 * 10^{13}$	$1.11 * 10^{13}$	$9.99 * 10^{11}$
20	0.03	0.5	$4.69 * 10^{14}$	$5.21 * 10^{13}$	$4.69 * 10^{12}$
20	0.03	1	$1.30 * 10^{14}$	$1.45 * 10^{13}$	$1.30 * 10^{12}$
20	0.03	2	$3.92 * 10^{13}$	$4.36 * 10^{12}$	$3.92 * 10^{11}$
20	0.01	0.5	$1.92 * 10^{14}$	$2.13 * 10^{13}$	$1.92 * 10^{12}$
20	0.01	1	$6.11 * 10^{13}$	$6.79 * 10^{12}$	$6.11 * 10^{11}$
20	0.01	2	$2.19 * 10^{13}$	$2.43 * 10^{12}$	$2.19 * 10^{11}$
10	0.1	0.5	$7.47 * 10^{14}$	$8.30 * 10^{13}$	$7.47 * 10^{12}$
10	0.1	1	$2.00 * 10^{14}$	$2.22 * 10^{13}$	$2.00 * 10^{12}$
10	0.1	2	$5.66 * 10^{13}$	$6.29 * 10^{12}$	$5.66 * 10^{11}$
10	0.03	0.5	$2.61 * 10^{14}$	$2.90 * 10^{13}$	$2.61 * 10^{12}$
10	0.03	1	$7.85 * 10^{13}$	$8.72 * 10^{12}$	$7.85 * 10^{11}$
10	0.03	2	$2.62 * 10^{13}$	$2.91 * 10^{12}$	$2.62 * 10^{11}$
10	0.01	0.5	$1.22 * 10^{14}$	$1.36 * 10^{13}$	$1.22 * 10^{12}$
10	0.01	1	$4.38 * 10^{13}$	$4.86 * 10^{12}$	$4.38 * 10^{11}$
10	0.01	2	$1.75 * 10^{13}$	$1.95 * 10^{12}$	$1.75 * 10^{11}$

Table 1: Table of accuracy for the required amount of protons needed for different parameters.

3.2 Analysing the behavior of two PET detectors when switched off and on

3.2.1 Energy calibration

The program Mesytec has been used to analyse the behavior of a PET detector when it is switched off for $10ms$ and afterwards switched on. First of all, an energy calibration was done. Two detectors, named detector 5 and 7, were used for the measurements. The energy was not calibrated yet. Therefore, measurements of a ^{22}Na source, having two energy peaks of respectively $511keV$ and $1275keV$, were used to calibrate both detectors. A graph was made with the number of counts as function of the energy, where the energy is given

in channel number. For detector 5, the energy spectrum is given in figure 17. Two gaussian functions on top of a linear background have been fit through the 511 and 1275keV peaks. This has been done using python. The code for the script is given in the appendix. The 511 and 1275keV peaks have been determined at a position 365.57 and 960.29. By making a graph of this, having a linear fit ($y = ax + b$) through these points, values for a and b can be found. This graph is shown in figure 18. The values for a and b have been determined to be 1.2846 for a and 41.375 for b.

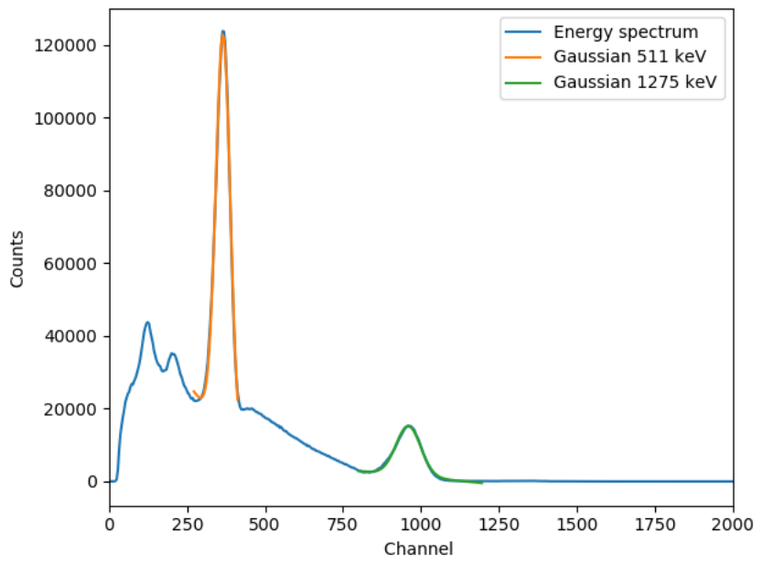

Figure 17: Energy spectrum for detector 5, expressing the energy in units of channel.

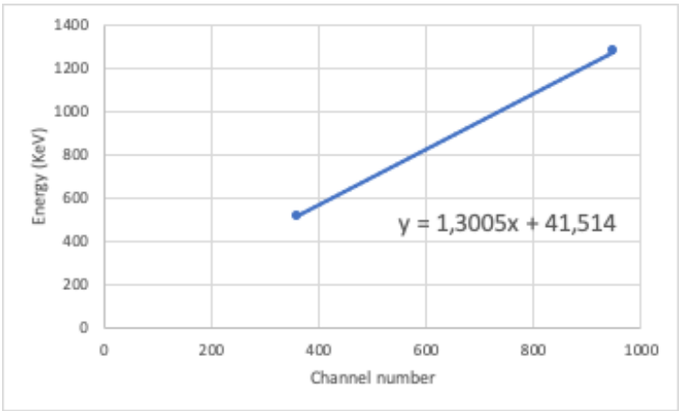

Figure 18: Energy calibration for detector 5, having a linear fit in the form y=ax+b.

The same procedure has been done for detector 7. The results are shown in figure 19 and 20. The 511 and 1275keV peaks have been determined at a position 361.00 and 948.46. Therefore, using these numbers, the values for a and b have been determined to be 1.3005 for a and 41.514 for b.

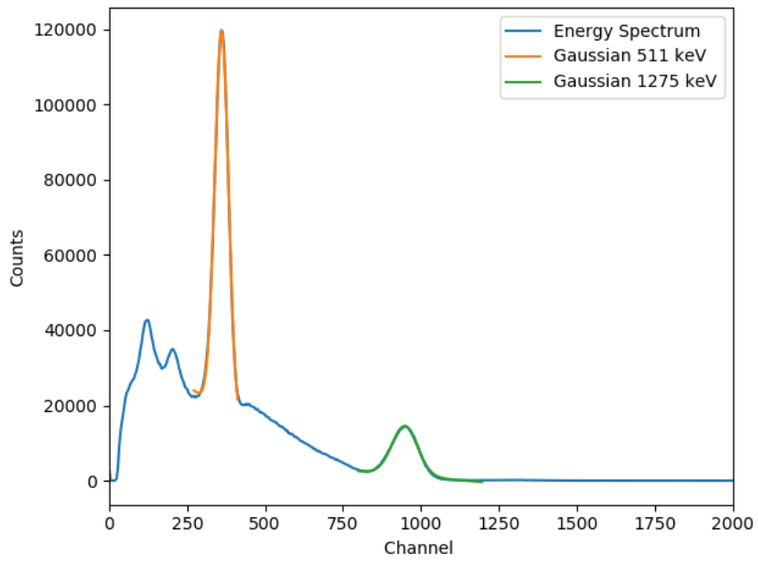

Figure 19: Energy spectrum for detector 7, expressing the energy in units of channel.

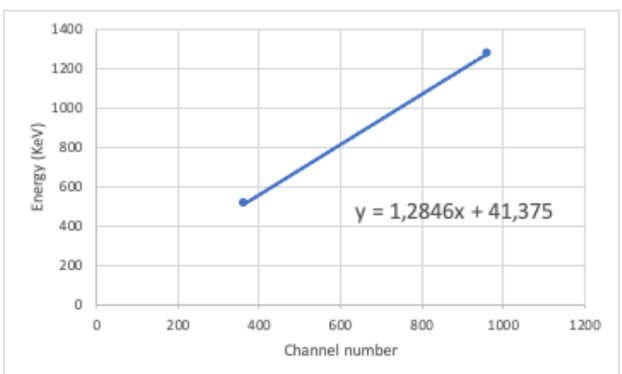

Figure 20: Energy calibration for detector 7, having a linear fit in the form y=ax+b.

3.2.2 2D plots for different ^{68}Ge sources

The behavior of the PET detector has been analysed when it is switched off and on. This has been done by taking measurements with three different sources and one measurement set without source. This was done because different count rates were wanted. Therefore, different sources were used because of the different intensities between the sources. The following sources are used: Listfile 4 did not contain any source, listfile 5 contained a ^{68}Ge point source, listfile 6 was taken with a ^{68}Ge vertical line source and listfile 7 did contain a ^{68}Ge vertical and horizontal line source plus point source. Furthermore, the detector was turned off at 20ms, and turned on at 30ms. The total loop had a duration of 100ms. This loop was repeated many times and the data was accumulated. The listfile measurements can be seen in figure 21, having detector 5 at the left and detector 7 at the right side, having listfile 4 at the top and listfile 7 at the bottom of the figure. These 2D histograms have the energy on the x-axis and time on the y-axis. Additionally, the color in the plot denotes the amount of counts measured, where red stands for maximum. White denotes zero counts and blue has a minimum of one count. Therefore, the red line is the 511keV photon peak. From figure 21, it can be seen that there is a curve in the red line between 30 and 50ms. This implies that the 511keV photon peak has shifted slightly to the left, giving a lower value of energy. Because of this, it can be concluded that the detectors have a recovery period when it is turned back on and do not work optimally during this period.

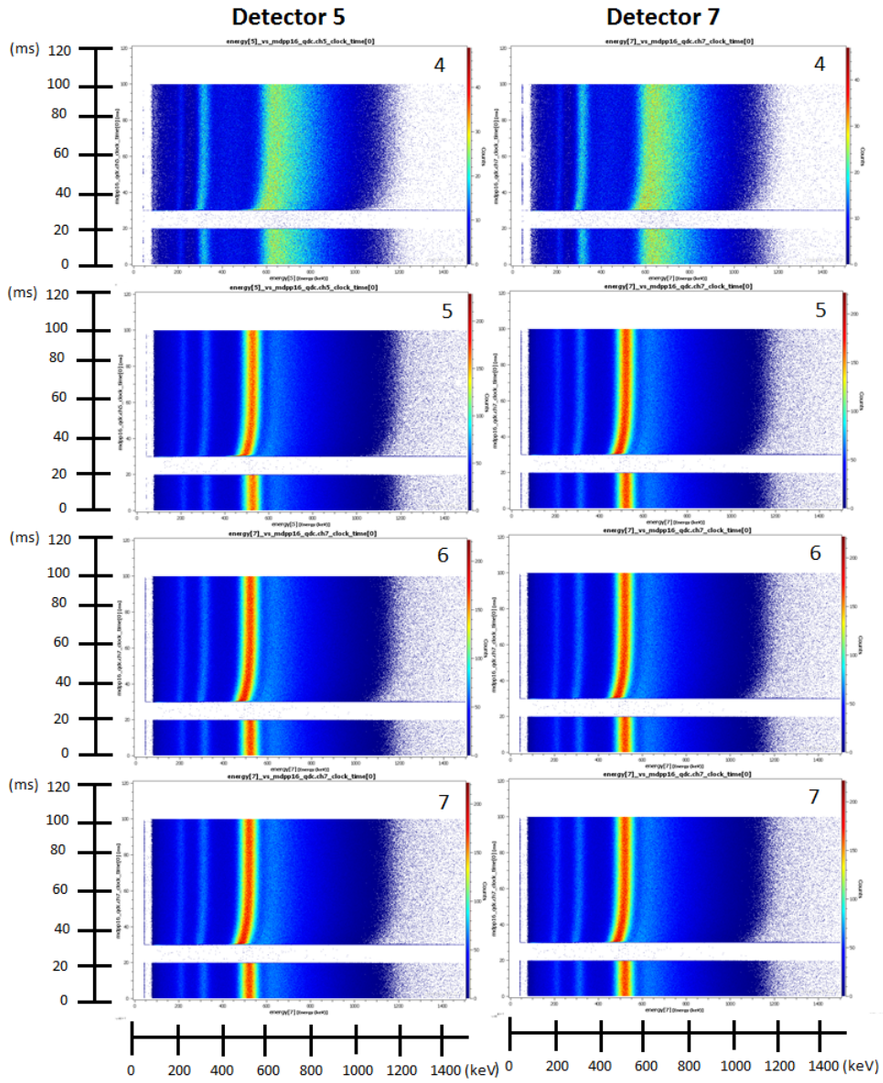

Figure 21: Behavior of detector 5 and 7 for four different sources when detector is switched off and on.

Furthermore, listfile 4 did not contain a source and only background radiation was measured. However, there is a decent number of counts at $511keV$. This can be explained to the fact that ludetium inside the LSO scintillator is radioactive.

3.2.3 Analysing the recovery effect for different energy windows

Furthermore, an analysis has been done for different energy windows. Range filters have been made for energies $435-650$, $445-650$, $455-650$, $465-650$ and $475-650keV$. Only the left part of the energy window was increased by $10keV$. The range filters were made for both detectors. Thereafter, a condition filter was made which only registers counts when both detectors measure it simultaneously within the mentioned range. A 1D histogram was made for for each energy window as function of time. The data has been imported in Matlab. The data measurements from 31 to $101ms$ were taken, since this is the topic of interest. By using Matlab, a cuvefit was made through the measurements. The form of the fit is given by equation (10). Matlab will generate the best estimated values for constants c , d and a. Parameter c is a constant, d is the intensity of the term $(1-exp)$. a is a parameter for τ, the recovery time. The best estimated parameters for the fits are shown in table 2.

$$curvefit = c + d * (1 - exp(-(x-31)/a)) \tag{10}$$

Energy window	$a \pm \sigma$	$c \pm \sigma$	$d \pm \sigma$
$435 - 650$	5.67 ± 1.14	938.5 ± 7.2	55.56 ± 7.06
$445 - 650$	6.01 ± 0.65	875.2 ± 6.9	100.10 ± 6.77
$455 - 650$	6.46 ± 0.39	775.0 ± 6.5	173.80 ± 6.40
$465 - 650$	6.95 ± 0.25	631.8 ± 6.2	276.40 ± 6.08
$475 - 650$	7.73 ± 0.18	457.5 ± 5.6	388.20 ± 5.48

Table 2: Best estimated parameters a,c and d for the fit for every energy window.

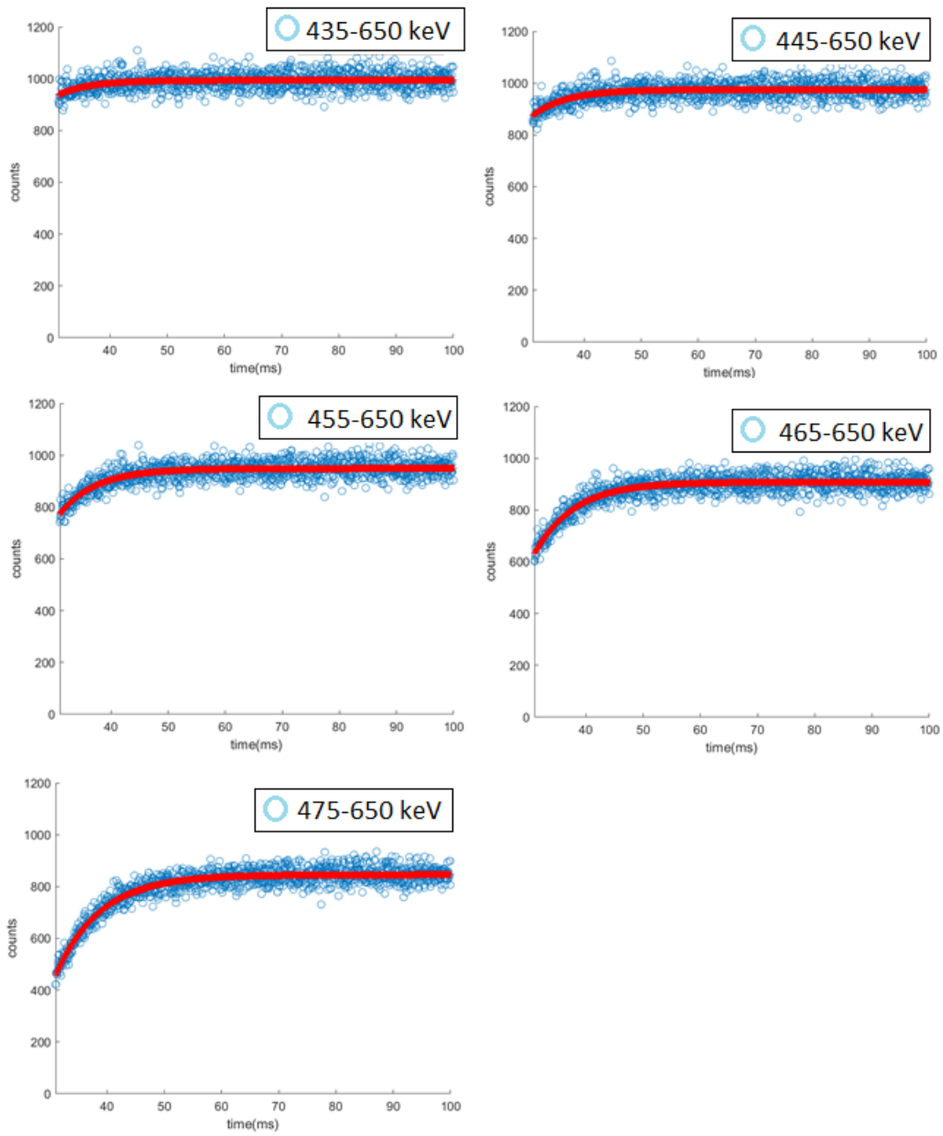

Figure 22: Counts as function of time for different energy windows with a best fit through the measurements.

In figure 22, the fits through the measurements for different energy windows can be seen. From the graph, it can be seen that the recovery effect is the greatest for energy window $475 - 650$ and decreases for bigger energy windows.

3.2.4 Analysing the behavior of the PET detectors in the recovery period

An analysis has been done for the recovery time for the detector between 30 and $55.5ms$. This recovery period is divided into two phases, a fast and slow recovery phase. Between $30 - 30.5ms$, the fast recovery phase was graphed, having steps of $0.1ms$. The slow recovery period was between $30.5 - 55.5ms$, having steps of $5ms$. The fast recovery can be seen in figure 23. From the graph, it can be seen that the signal is very unstable between $30.0 - 30.2ms$. Between $30.2 - 30.4ms$, the peak is slowly returning, but still contains a lot of noise. From $30.4ms$, the signal is almost stable but the peak is not positioned at $511keV$ yet.

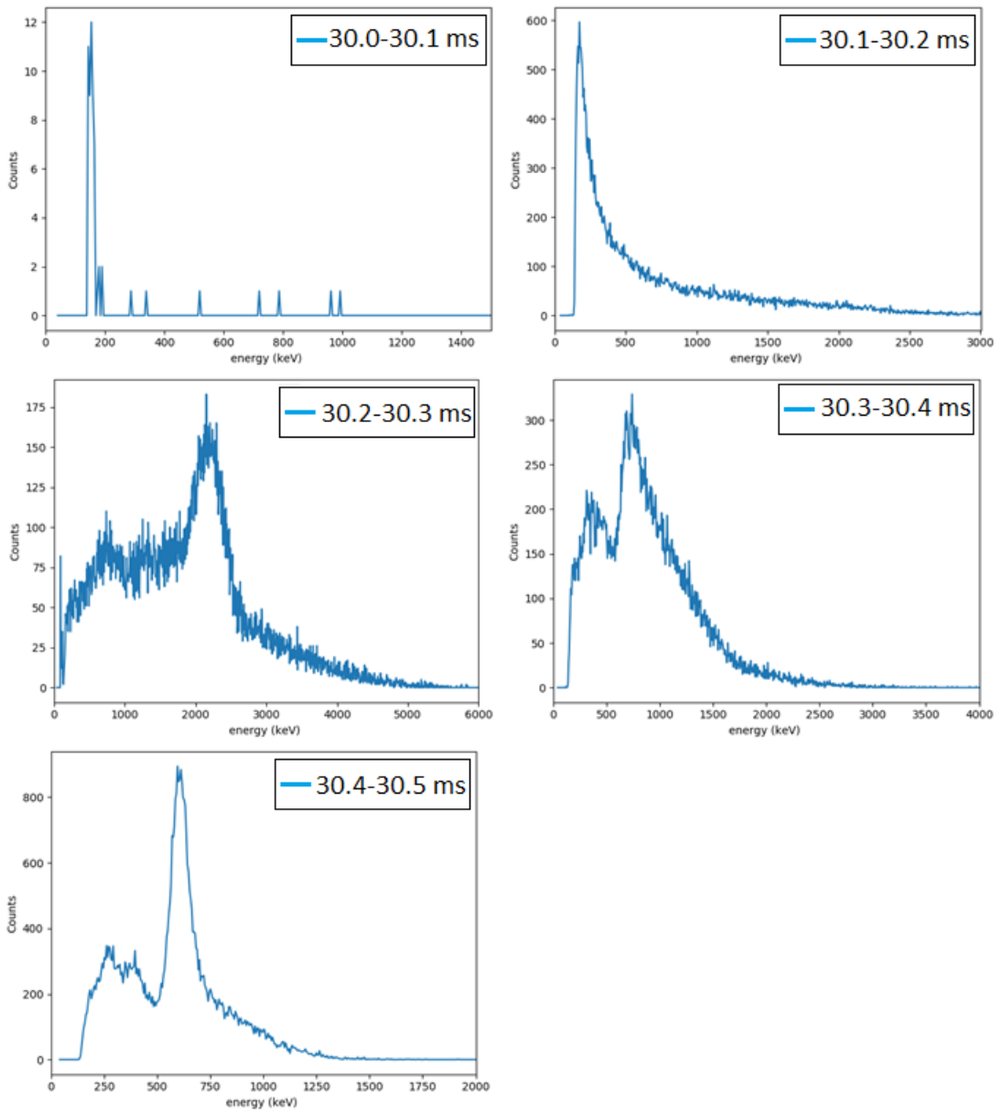

Figure 23: Energy spectrum in the fast recovery period of the detector between 30.0-30.5 ms with steps of $0.1ms$.

For the slow recovery, between $30.5 - 55.5ms$, one graph with all peaks for every time window has been made. This was done to show that the $511keV$ peak is positioned at a lower energy and slowly shifts back to its original location. The graph can be seen in figure 24.

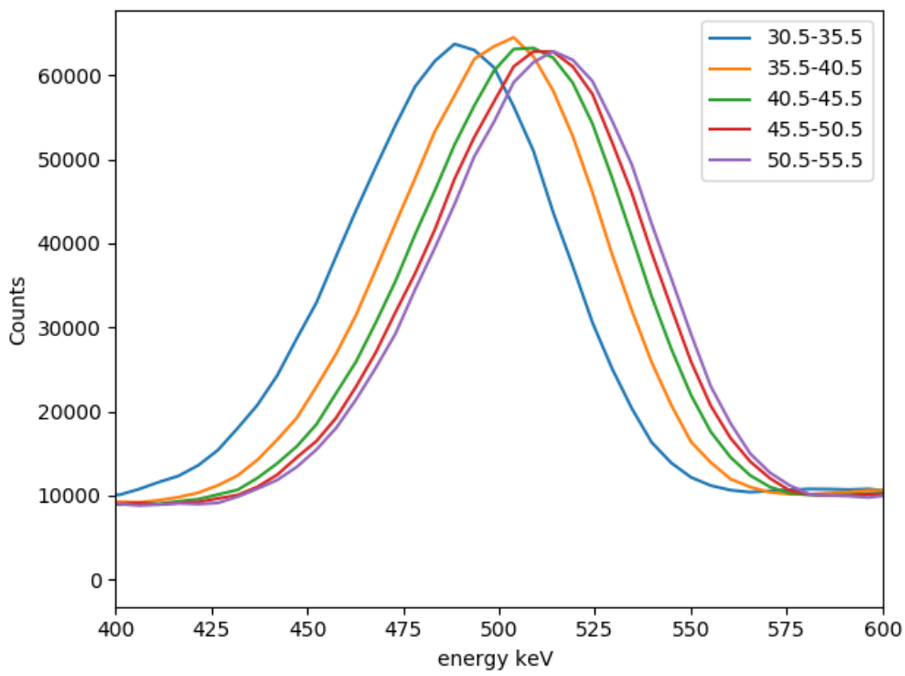

Figure 24: Energy spectrum of the peak position for different time periods in the slow recovery.

It can be concluded from the graph that the peak from the first time window is located at the lowest energy. For consecutive time windows, the peak slowly moves back to the place where it should be, namely $511keV$. The location of the peak of every time window can be seen in table 3. During this slow recovery period, the signal is stable but the gain is not optimal yet.

Time window (ms)	peak location (keV)
$30.5 - 35.5$	488.1
$35.5 - 40.5$	499.6
$40.5 - 45.5$	506.0
$45.5 - 50.5$	509.9
$50.5 - 55.5$	512.4

Table 3: Peak location of every time window for the slow recovery.

4 Discussion

4.1 Beam time plan for the detection of $4.44MeV$ gamma rays

The results of table 1 can be used to make a beam time plan to execute the physical experiment. The proton beam used in this physical experiment will be pulsed. This could be done by series of $10ms$ of beam-on $90ms$ beam-off. The accelerator could generate among other things pulses consisting of 10^8 and 10^9 protons per pulse [3]. Using this beam intensity and beam-on and beam-off time, the target could be irradiated with 10^9 and 10^{10} protons per second. By looking at table 1, to achieve a relative accuracy of 1% and have a carbon target of $1mm$ and use the assumptions that the water region thickness is $20cm$ and cross section for water is 0.1, $3.73 * 10^{14}$ protons are required. This would imply that the beam time of this experiment is at least 10 hours with an intensity of 10^{10} protons per second. This duration is too long. For the same parameters but a 3% relative accuracy, $4.15 * 10^{13}$ protons are required, which will result in a beam time of approximately $70min$, which is a more appropriate beam time for this experiment. Furthermore, it is uncertain if the NaI detector could function properly with this beam intensity. A possible solution for the long beam time would be to change the beam-off time. By making this twice as short, the total beam time will almost be twice as short.

4.2 Determination of the proton energy as a function of depth in water

The proton energy as a function of depth in water has been determined. This has been done using the stopping power [4]. The following steps have been taken for the stopping power of specific energies: $1MeV$ have been taken for the values ranging from 0 to $40MeV$, steps of $2MeV$ between 40 to $120MeV$ and steps of $5MeV$ between 120 to $180MeV$. For example, for an energy of $123MeV$, the stopping power of $125MeV$ ($6.192\frac{MeVcm^2}{g}$) was used instead of the specific stopping power of $123MeV$ ($6.264\frac{MeVcm^2}{g}$). Although this is a relatively small difference, and the energy of interest is in the Bragg peak range, this will give slightly different outcomes eventually. Therefore, an improvement for this work would be to use the specific stopping power for every energy, instead of rounding off. This would give a more accurate answer.

4.3 The $^{12}C(p,n)^{12}N$ Cross section

For the determination of production rate of $4.44MeV$ gamma rays created by ^{12}N, the cross section of this reaction is needed. The cross section has been taken from Rimmer and Fisher (1968) [7]. This paper gives the cross section for values up to $48MeV$. The cross section for $48MeV$ has been determined to be $2.3mb$. Since the cross section was slowly decreasing, from $48MeV$ to $56MeV$, the cross section was estimated to decrease to $2mb$. From $56MeV$ to $190MeV$, the value $2mb$ was taken. Therefore, the production rate is equal for all energies in the range from $56MeV$ to $190MeV$. An improvement in this experiment would be to do measurements regarding this cross section for energies between $48MeV$ and $190MeV$. This would give more accurate results for the production of $4.44MeV$ gamma rays in carbon at energies higher than $48MeV$.

4.4 Region in water for which the NaI detector can measure $4.44MeV$ gamma rays

The detector measures the production from a distance of $25cm$ from the target. There is no explicit value for the region over which the detector can detect. Therefore, lines have been drawn through the detector to estimate this region. This was shown in figure 4. The region was measured to be $21.7cm$. The lines were taken from the sides in the middle of the scintillator. For two different regions, namely 10 and $20cm$, measurements have been done. However, it could be possible that this measured distance is too small. If lines are drawn from the top of the scintillator, moving past the edges of the housing, the region would be bigger than assumed. Therefore, an improvement of this work would be to determine the region for which the detector is working properly at a distance of $25cm$ from the target. Furthermore, the region of the detector in water cannot exceed the range of the protons. In the future, another experiment could be planned having a proton beam with an initial energy of $90MeV$. Protons with this energy will travel approximately $64mm$ before they come to rest. This experiment will be done because the straggling (energy spread) is bigger at the carbon target for an initial $190MeV$ than for $90MeV$. Expected is that this experiment with an initial $90MeV$ proton beam will give results with a better resolution. Additionally, lead shielding could be placed between the box filled with water and the detector. This

could prevent the detection of a part of the gamma rays created in water. Besides, this shielding will be done such that it does not decrease the efficiency of the irradiation in the carbon target.

4.5 Analysis of the behavior of the PET detectors

For the energy windows varying between 435-475 with upper limit 650 keV, a best fit has been made through the measurements. All data between $0 - 31ms$ has been expelled, to make a best fit. Furthermore, Matlab was used to make a curvefit in the form of equation (10). From the graphs in figure 25, it can be seen that the curve becomes more to a horizontal line as the energy window increases. This indicates that a bigger energy window is less affected by the recovery effect. If the data is horizontal and thus constant, the signal is stable. The smallest energy window, $475 - 650keV$, is the most affected by the recovery effect and therefore has the biggest curve in the fit. From figure 24 and 27, it can be seen that the peak position is shifted when the detectors were switched on. The $511keV$ peak was positioned lower, up to a value of $488keV$. From figure 27, it can be seen that there are counts in the range from $425 - 450keV$. If the energy window is set to $475 - 650keV$, these counts will not be registered, resulting in a decrease of counts until the signal is stable again. Thus it can be concluded from this information that there is a stronger recovery effect for smaller energy windows.

4.6 Determination of the 511 keV peak for slow recovery

The position of the $511keV$ peak has been determined for the slow recovery, varying between 30.5 and $55.5ms$. The result obtained can be seen in figure 24 and the peak locations are given in table 3. For the last time window $50.5 - 55.5ms$, the peak location was determined to be $512.4keV$. This indicates that the peak location is higher than it should be, namely $511keV$. The measurements with a ^{22}Na source were recorded short before the measurements with the different Ge sources were done. The calibration was done with the data sets of the ^{22}Na source because of the $511keV$ and $1275keV$ peak. This calibration was used for the analysis of the Ge source. However, because of the time difference between the ^{22}Na and ^{68}Ge measurements, this calibration could be different for both. This would mean that the peak locations of the ^{68}Ge measurements are slightly different than it was defined now. An improvement for this experiment would be to do another measurement with the ^{22}Na after the measurements with the ^{68}Ge. By comparing the calibration measurements done before and after the real experiment, more clarity could be given to the accuracy of the calibration.

5 Conclusion

In this work, the amount of protons required to obtain a specific relative accuracy in the detection of $4.44MeV$ gamma rays has been determined. The required number of protons is needed to make a beam time plan, including the time of irradiation and the amount of protons that forms the beam. The determination was done at a depth of $220mm$. The analysis has been done for three different carbon target thicknesses. The gamma ray detector was positioned a distance of $25cm$ from the target. Furthermore, since the region of detection for the gamma ray detector is not known exactly, this analysis was done for a region of $10cm$ and $20cm$. In addition, it is known that the cross section of water is at least ten times smaller than the cross section of carbon. Therefore three different cross sections have been taken for water, of approximately 10%, 3% and 1% of the carbon CS. To obtain a relative accuracy of 1%, a too long beam time would be needed presumably. Consequently, it would be better to execute this experiment and obtain a relative accuracy of 3% . Improvements on this research would be to find a specific value for the region in water for which the gamma-ray detector could measure. Furthermore, measurements could be done regarding the cross section of $^{12}C(p,n)^{12}N$ in water.
Furthermore, the behavior of a PET-detector has been analysed when it was switched off and on. The recovery effect was analysed for different energy windows. It can be concluded that the recovery effect is the greatest for the smallest energy window. In addition, it can be concluded that the recovery period can be divided into two phases. From $30.0 - 30.5ms$, there is a fast recovery phase. During this period, the signal is unstable. From $30.5 - 55.5ms$, the slow recovery phase is active and a shift in the $511keV$ peak is observable. This is measured at $488.1keV$ for time window $30.5 - 35.5ms$. At a time window of $50.5 - 55.5ms$ the peak has been restored.

6 Acknowledgements

The author is grateful to Peter Dendooven for his help with this research project.

References

[1] Studenski MT, Xiao Y, Proton Therapy dosimetry using positron emission tomography, World journal of radiology, april 2010

[2] Kuno Y, Okada Y, Muon decay and physics beyond the standard model, Institute of Particle and Nuclear Studies (IPNS), september 1999

[3] Ozoemelam I, van der Graaf E R, Goethem M-J, Kapusta M, Zhang N, Brandenburg S, Dendooven P, Feasibility of Quasi-Prompt PET-based Range Verification in Proton Therapy, december 2019, KVI-Center for Advanced Radiation Technology of the University of Groningen

[4] https://physics.nist.gov/PhysRefData/Star/Text/PSTAR.html

[5] van der Graaf E R, Detector efficiency simulations Efficiencies for a 91x91x150 mm NaI detector in the Eurogam clover detector housing, Februari 2020, KVI-Center for Advanced Radiation Technology of the University of Groningen

[6] Zhu X, El Fakhri G, Proton Therapy Verification with PET Imaging, Ivyspring, september 2013, Center for Advanced Medical Imaging Sciences

[7] Rimmer E M, Fisher P S, Resonances in the (p,n) reaction on 12C, 1968, Nuclear Physics A 108 561-6

[8] Dang H, Particle Induced strand breakage in plasmid DNA, november 2010, University of Groningen

[9] Polf J C, Parodi K, Imaging particle beams for cancer treatment, october 2015, Physics today

[10] Martin B R, Shaw G, Nuclear and Particle physics An Introduction, third edition, 2009, Wiley, page 23-25

[11] Klein-Douwel R J H, Physics laboratory 1 Data and error analysis, 2019-2020, University of Groningen

[12] Cherry S R, Sorenson J A, Phelps M E, Physics in Nuclear Medicine, fourth edition, 2012, Elsevier, page 307-323

[13] Barclay D L, A statistical note on trend factors: The meaning of "R-squared", march 1989, Casualty Actuaries of the Northwest

[14] Knoll G F, Radiation Detection and Measurement, third edition, 1999

[15] Med Phys, Radioisotopes and Radiation Methodology, Chapter 4 Scintillation Detectors, Med Phys 4R06/6R03

[16] Birks J B, The Theory and Practice of scintillation counting, first edition, January 1964, Pergamon Press Ltd

[17] Dendooven P, Buitenhuis H J T, Diblen F, Heeres P N, Biegun A K, Fiedler F, van Goethem M-J, van der Graaf E R, Brandenburg S, Corrigendum: short-lived positron emitters in beam-on PET imaging during proton therapy, 2015, Phys. Med. Biol.60 8923

[18] Flyckt S O, Marmonier C, Photomultiplier Tubes principles and applications, 2002, photonis, France

[19] Schmitz R E, Alessio A M, Kinahan P E, The physics of PET/CT scanners, 2013, Department of Radiology, University of Washington

[20] Zanzonico P, Positron Emission Tomography: A Review of Basic Principles, Scanner Design and Performance, and current systems, 2004, Elsevier, New York

[21] Ferrero V, Fiorina E, Morrocchi M, Pennazio F, Baroni G, Battistoni G, Belcari N, Camarlinghi N, Ciocca M, Guerra A D, Donnetti M, Giordanengo S, Giraudo G, Patera V, Peroni C, Rivetti A, da Rocha Rolo M D, Rossi S, Rosso V, Sportelli G, Tampellini S, Valvo F, Wheadon R, Cerello P, Bisogni M G, Online proton therapy monitoring: clinical test of a silicon-photodetector-based-in-beam PET, March 2018, Scientific Reports

[22] van der Graaf E R, HPGe detector simulations Efficiencies for the Eurogam clover detector, June 2016, KVI-Center for Advanced Radiation Technology of the University of Groningen

[23] Paganetti H, Range uncertainties in proton therapy and the role of Monte Carlo simulations, may 2012, Phys Med Biol 57 R99-R117

[24] Kelley J H, Purcell J E, Sheu C G, Energy levels of light nuclei A = 12, July 2017, page 164-165, Nuclear Physics A 968(2017) 71-253, Elsevier

[25] https://www.nndc.bnl.gov/nudat2/decaysearchdirect.jsp?nuc=12Nunc=nds

[26] Etile A, Denis-Petit D, Gaudefroy L, Meot V, Roig O, A gated LaBr3(Ce) detector for border protection applications, 2018, Nuclear Instruments and Methods in Physics Research Section A 877, pages 323-327

[27] Hara K, Harada H, Toh Y, Hori J, Gamma-flash suppression using a gated photomultiplier assembled with an LaBr3(Ce) detector to measure fast neutron capture reactions, 2013, Nuclear Instruments and Methods in Physics Research Section A 723, pages 121-127

[28] Peter Dendooven, private communication

7 Appendix

7.1 Gaussian fitting for the calibration

```python
import matplotlib.pyplot as plt
from scipy.optimize import curve_fit
import numpy as np

def readData(filename):
    fh = open(filename)
    (line_cnt, xmin, xmax, _, _) = map(int, fh.readline().split(' '))
    x = [0] * line_cnt
    y = [0] * line_cnt
    for i in range(0, line_cnt):
        x[i] = 4*i
        y[i] = int(fh.readline().rstrip())

    return np.array(x), np.array(y)


def Gauss(x, a, x0, sigma, b, c):
    return (b+c*x+(a * np.exp(-(x - x0)**2 / (2 * sigma**2))));

def plotGaussian(x, y, label='fit'):
    b = 0
    c = 0
    mean = (sum(x * y) / sum(y))
    sigma = np.sqrt(sum(y * (x - mean) ** 2) / sum(y))
    popt, pcov = curve_fit(Gauss, x, y, p0=[max(y), mean, sigma, b, c])
    print(popt)
    plt.plot(x, Gauss(x, *popt), label=label)



#x, y = np.loadtxt('Energy_7_8192.txt', delimiter=' ', unpack=True)
x, y = readData('energy[5]_total_if_mdpp16_qdc.ch5_clock_time_outside_range_20-50.txt')
```

Figure 25: Python code of the gaussian curve through the 511 and 1275keV peak

```python
x, y = readData('energy[5]_total_if_mdpp16_qdc.ch5_clock_time_outside_range_20-50.txt')

peak1_x = x[68:104]
peak1_y = y[68:104]

peak2_x = x[200:300]
peak2_y = y[200:300]

plt.plot(x, y, label='Energy spectrum')
plotGaussian(peak1_x, peak1_y, label='Gaussian 511 keV')
plotGaussian(peak2_x, peak2_y, label='Gaussian 1275 keV')
plt.legend()
# plt.title('Fig. 3 - Fit for Time Constant')
plt.xlabel('Channel ')
plt.ylabel('Counts')
plt.show()
plt.savefig('Energyplot5.2.png')
```

Figure 26: Python code of the gaussian curve through the 511 and 1275keV peak

7.2 Determination of the $511keV$ peak for the slow recovery

```python
import matplotlib.pyplot as plt
from scipy.optimize import curve_fit
import numpy as np

def readData(filename):
    fh = open(filename)
    (line_cnt, xmin, xmax, _, _) = map(int, fh.readline().split(' '))
    x = [0] * line_cnt
    y = [0] * line_cnt
    for i in range(0, line_cnt):
        x[i] = 1.2846 * (4*i) + 41.375
        y[i] = int(fh.readline().rstrip())

    return np.array(x), np.array(y)


def Gauss(x, a, x0, sigma, b, c):
    return (b+c*x+(a * np.exp(-(x - x0)**2 / (2 * sigma**2))));

def plotGaussian(x, y, label='fit'):
    b = 0
    c = 0
    mean = (sum(x * y) / sum(y))
    sigma = np.sqrt(sum(y * (x - mean) ** 2) / sum(y))
    popt, pcov = curve_fit(Gauss, x, y, p0=[max(y), mean, sigma, b, c])
    print(popt)
    plt.plot(x, Gauss(x, *popt), label=label)



#x, y = np.loadtxt('Energy_7_8192.txt', delimiter=' ', unpack=True)
x, y = readData('energy[5]_if_mdpp16_qdc.ch5_clock_time[0]_30.5-35.5_slow1106.txt')
```

Figure 27: Python code for the determination of the $511keV$ peak

```python
x, y = readData('energy[5]_if_mdpp16_qdc.ch5_clock_time[0]_30.5-35.5_slow1106.txt')
x2, y2 = readData('energy[5]_if_mdpp16_qdc.ch5_clock_time[0]_35.5-40.5_slow1106.txt')
x3, y3 = readData('energy[5]_if_mdpp16_qdc.ch5_clock_time[0]_40.5-45.5_slow1106.txt')
x4, y4 = readData('energy[5]_if_mdpp16_qdc.ch5_clock_time[0]_45.5-50.5_slow1106.txt')
x5, y5 = readData('energy[5]_if_mdpp16_qdc.ch5_clock_time[0]_50.5-55.5_slow1106.txt')

peak1_x = x5[70:112]
peak1_y = y5[70:112]

plt.plot(x, y, label='30.5-35.5')
plt.plot(x2, y2, label='35.5-40.5')
plt.plot(x3, y3, label='40.5-45.5')
plt.plot(x4, y4, label='45.5-50.5')
plt.plot(x5, y5, label='50.5-55.5')
plotGaussian(peak1_x, peak1_y, label='peak1')

plt.legend()
# plt.title('Fig. 3 - Fit for Time Constant')
plt.xlabel('energy keV ')
plt.ylabel('Counts')
plt.xlim(300, 700)
plt.show()
```

Figure 28: Python code for the determination of the $511keV$ peak